PAPER

Check for updates

Tailoring NiCoCu layered double hydroxide with Ag-citrate/polyaniline/functionalized SWCNTs nanocomposites for supercapacitor applications†

Syed Muhammad Abdullah, [a] Mohsin Ali Marwat, ‡*[a] Kanwar Muhammad Adam,[a] Zia Ud Din,[a] Muhammad Humayun,[b] Muhammad Ramzan Abdul Karim, [a] Esha Ghazanfar,[a] Mohamed Bououdina,[b] Umaima Hamayun,[a] Mahmoud Saber Youssef[c] and Hafiz Tauqeer Ali[c]

Supercapacitors have substantially altered the landscape of sophisticated energy storage devices with their exceptional power density along with prolonged cyclic stability. On the contrary, their energy density remains low, requiring research to compete with conventional battery storage devices. This study addresses the disparities between energy and power densities in energy storage technologies by exploring the integration of layered double hydroxides (LDH) and highly conductive materials to develop an innovative energy storage system. Four electrodes were fabricated *via* a hydrothermal process using NiCoCu LDH, Ag-citrate, PANI, and f-SWCNTs. The optimal electrode demonstrated exceptional electrochemical properties; at 0.5 A g^{-1}, it possessed specific capacitances of 807 F g^{-1}, twice as high as those of the pure sample. The constructed asymmetric supercapacitor device attained energy densities of 62.15 W h kg^{-1} and 22.44 W h kg^{-1}, corresponding to power densities of 1275 W kg^{-1} and 11 900 W kg^{-1}, respectively. Furthermore, it maintained 100% cyclic stability and a coulombic efficiency of 95% for 4000 charge−discharge cycles. The concept of a supercapacitor of the hybrid grade was reinforced by power law investigations, which unveiled *b*-values in the interval of 0.5 to 1. This research emphasizes the considerable potential of supercapacitor-grade NiCoCu LDH/Ag-citrate−PANI−f-SWCNTs nanocomposites for superior rate performance, robust cycle stability, and enhanced energy storage capacity.

1. Introduction

A perpetual desire for energy is the distinguishing characteristic of the current period.[1,2] Energy storage solutions that are ecologically safe and efficient are more important than ever since they power rising cities and our ever-present electronics. Supercapacitors, which combine the best of batteries and capacitors, are strong contenders in this competition.[3,4] In contrast to batteries, supercapacitors store energy electrically as opposed to chemically.[5–7] Charge and discharge cycles are faster and last longer. They lessen environmental consequences and improve safety in applications that require rapid energy delivery

[a]Faculty of Materials and Chemical Engineering, Ghulam Ishaq Khan (GIK) Institute of Engineering Sciences and Technology, Topi, 23640, Pakistan. E-mail: mohsin.ali@giki.edu.pk; Fax: +92-938-281032; Tel: +92-938-281026

[b]Energy, Water, and Environment Lab, College of Humanities and Sciences, Prince Sultan University, Riyadh, 11586, Saudi Arabia

[c]Department of Mechanical Engineering, College of Engineering, Taif University, Kingdom of Saudi Arabia

and big power spikes, which batteries always have. As we electrify and switch to renewable energy, supercapacitors are becoming more important.[8] Their energy storage and release capabilities may improve grid stability, renewable energy system power variations, and electric car utilization. Supercapacitor technology's scalability and diversity provide exciting new applications in consumer electronics, grid-scale energy storage, and aerospace.[9,10]

The technology in supercapacitors is adapted to individual needs. Electronically separated ions form a double layer at the electrode–electrolyte interface in electrochemical double-layer capacitors (EDLCs). High power densities, low energy densities. While possessing high power densities, they have restricted energy densities.[11,12] On the contrary, pseudocapacitors store energy on the electrode material *via* faradaic redox reactions; this leads to increased energy densities but reduced power densities.[13–16] Hybrid supercapacitors, as their name suggests, integrate the most advantageous characteristics of pseudocapacitors (pseudocapacitors) and electrolyte drop capacitors (EDLCs) to attain an equilibrium between energy and power densities.[17–19] As the performance of these devices is highly dependent on the electrode material, scientists are developing

novel composites and materials to enhance the capabilities of supercapacitors. There are several materials that may be utilized as electrodes in supercapacitors, each with distinct advantages and disadvantages. In contrast to metal–organic frameworks (MOFs),[20–22] which can alter their structures and possess expansive surfaces, layered double hydroxides (LDHs) are exceptionally stable and cyclable in the environment.[23] The pseudocapacitive characteristics of transition metal phosphates, sulfides, and oxides can be attributed to their intricate redox chemistry.[24] LDHs are multi-metal clays. Brucite layers with metal cations create $M^{2+}(OH)_6/M^{3+/4+}(OH)_6$ octahedra.[25] These electrode materials are attractive due to their strong redox activities, environmental friendliness, and efficient usage of evenly distributed transition metal atoms.[26] They have fascinating electrochemical and electrical properties due to their facile layer adjustment of cations and ability to exchange anions without affecting the structure. Different from conventional metal hydroxide-based electrodes, they can be easily exfoliated into monolayer nanosheets and chemically changed. In recent years, LDH electrochemical behavior studies have increased due to these unique properties.[27–30] The theoretical capacitance of nickel and cobalt exceeds 2000 F g^{-1}, making them ideal for pseudocapacitance.[31,32] Other transition metals like Fe, Mn, and Cu are electrochemically active. In NiFe-LDH, replacing Ni with Cu increases proton absorption and catalytic efficiency. Cu in Ni or Co-based LDH increases specific surface area, capacitance, and rate capability, improving electrochemical characteristics.[33] More active metal ions with higher valence states increase capacitive properties and electron transport in LDHs by reducing equivalent series resistance. Multi-active metal hydroxides' homogeneous element distribution may improve electroactive site use. These reasons led us to use NiCoCu LDH as pristine material. In order to increase LDHs' electrochemical performance, graphene oxides, carbon nanotubes (CNTs), carbon nanofibers (CNFs), nanowires, and conducting polymers have been added. After 2000 cycles, CNFs/Ag–NiCo-LDHs had 1133.3 mF cm^{-2} areal capacitance and 80.47% cyclic stability, according to Sekhar et al.[34] Yang et al. created NiCoAl-LDHs–MWCNT nanohybrids with loose nanostructures because they increase specific surface area and electrochemical characteristics.[35] A unique supercapacitor technique by Sara et al.[36] produced NiCo-LDH/G/PANI-NT@CC with 431.30 mF cm^{-2} areal capacitance and 84.05% cycling stability after 10 000 cycles.[37]

Despite the strong electrical conductivity and pseudocapacitive properties exhibited by conducting polymers such as polyaniline (PANI),[38] concerns persist over their structural stability. Auspicious carbon-based materials include functionalized single-walled carbon nanotubes (SWCNTs), which possess excellent electrical conductivity and a large surface area.[39] In order to surmount the constraints imposed by individual materials, scientists often employ synergistic composites. The ability to accurately regulate their surface chemistry and interfacial interactions through functionalization techniques can enhance charge storage capacity and electrochemical stability.[40] Innovative manufacturing techniques and scalable synthesis strategies are required to surmount

challenges such as aggregation-induced performance loss and scalability issues to ensure that carbon-based supercapacitor electrodes function as intended. As researchers strive to identify the ideal material for supercapacitors, they are increasingly exploring hybrid topologies and synergistic composites to overcome the limitations of individual materials and achieve improved performance metrics.[41] Synergistic composites exhibit enhancements in energy density, power density, and cycle stability. These improvements are achieved by meticulously integrating diverse components possessing complementary qualities. This creates opportunities for developing more advanced supercapacitor technologies capable of adapting to the evolving requirements of energy storage applications.[42]

In an effort to enhance charge storage processes, researchers endeavor to develop hierarchical structures and nano/microscale interfaces that optimize ion accessibility while minimizing the constraints imposed by diffusion.[43] Materials such as Co, Ni, Cu, SWCNT, and Ag are used in supercapacitor studies due to their superior electrochemical properties, which improve performance by offering high capacitance, excellent conductivity, and stability. When these materials are combined into a nanocomposite, they display synergistic effects. This research endeavor aims to fabricate an innovative composite electrode material for supercapacitors by integrating functionalized SWCNTs, NiCoCu-LDH, Ag-citrate, and PANI. The complementary qualities of each component support this determination. By using the redox activity of Ag ions, Ag-citrate promotes pseudocapacitive behavior and functions as a conductive binder, whereas NiCoCu-LDH possesses a substantial surface area and exceptional cyclability. PANI boosts the composite's specific capacitance and pseudocapacitive properties, whilst functionalized SWCNTs simplify charge transport and enhance electrical conductivity. Consequently, the ideal sample exhibited specific capacitances of 807 F g^{-1} at a current density of 0.5 A g^{-1}, which was twice as great as those of the pristine sample. At 1275 W kg^{-1} and 11 900 W kg^{-1}, the energy density of the asymmetric supercapacitor device was recorded as 62.15 W h kg^{-1} and 22.44 W h kg^{-1}, respectively. Moreover, it retained 100% capacity and a coulombic efficiency of 95% over 4000 cycles. Our hypothesis regarding a supercapacitor of hybrid grade was validated using power law analysis, which produced b-values in the range of 0.5 to 1. The results obtained from this research demonstrate that the NiCoCu LDH/Ag-citrate–PANI–f-SWCNTs nanocomposites exhibit remarkable rate stability, enhanced energy storage capabilities, and resilient cycle performance, rendering them very promising for implementation in supercapacitors.

2. Methodology

2.1 Raw materials

The following materials were purchased from Sigma-Aldrich: ethanol, acetone, silver nitrate ($AgNO_3$), cobalt nitrate hexahydrate ($Co(NO_3)_2 \cdot 6H_2O$), copper nitrate hexahydrate ($Cu(NO_3)_2 \cdot 6H_2O$), and nickel nitrate hexahydrate ($Ni(NO_3)_2 \cdot 6H_2O$). Neither of these was further purified or altered. Purchased from Honeywell (Germany) urea ($CO(NH_2)_2$), sodium citrate

($Na_3C_6H_5O_7$), pure 1-methyl-2-pyrrolidone (NMP), and deionized (DI) water was also utilized exactly as supplied, requiring no additional purification or alteration, Ni foam was used as substrate material. Following a functionalization method, single-walled carbon nanotubes (SWCNT) were acquired from Sigma Aldrich and utilized. The following materials were utilized and purchased from Sigma Aldrich and exactly as received: 98% sulfuric acid (H_2SO_4), 37% hydrochloric acid (HCl), and aniline ($C_6H_5NH_2$).

2.2 Synthesis of NiCoCu LDH

NiCoCu LDH was synthesized using a hydrothermal process. Initially, 1 mmol each of nickel nitrate hexahydrate ($Ni(NO_3)_2\cdot6H_2O$), cobalt nitrate hexahydrate ($Co(NO_3)_2\cdot6H_2O$), and copper nitrate hexahydrate ($Cu(NO_3)_2\cdot6H_2O$) were dissolved in 60 mL of DI water together with 3 mmol of urea ($CO(NH_2)_2$) to make a solution. A magnetic stirrer agitated the mixture for thirty minutes to ensure a homogeneous dispersion. The solution was subjected to hydrothermal treatment at 120 °C for 14 hours within an autoclave. Following the completion of the hydrothermal process, the autoclave reactor underwent controlled cooling to reach ambient temperature. The collected solid precipitates from the reactor vessel were subjected to a two-step washing process within a centrifuge. The mixture was first centrifuged with DI water at 4000 rpm for 10 minutes, followed by another 10-minute centrifugation with ethanol at the same speed. The final NiCoCu LDH product was obtained by vacuum drying the resultant-washed precipitate for eight hours at 60 °C. A comprehensive schematic illustrating the process of synthesizing NiCoCu LDH can be found in Fig. 1.

2.3 Synthesis of polyaniline (PANI)

The synthesis of PANI was initiated by dissolving 1 g of pure aniline (ANI) in 12.5 mL of a 1 M HCl acid solution under constant stirring in an ice bath.[44] Subsequently, 30 L of an acid-saturated ammonium persulfate (APS) solution was gradually added dropwise while maintaining a stoichiometric ratio of 1 : 1 (ANI : APS) to ensure complete polymerization. After six hours of magnetic stirring, a reaction mixture, the precipitated product was obtained. Furthermore, it was neutralized with distilled water and left to dry overnight. Acetone was used to purify the product, then dried for 24 hours at 80 °C. A comprehensive schematic illustrating the process of synthesizing PANI can be found in Fig. 1.

2.4 Functionalization of single-walled carbon nanotubes (SWCNT)

The following protocol was used when conducting acid functionalization experiments. 250 mL of 10 M H_2SO_4/HNO_3 (3 : 1 v/v) were mixed at the necessary concentrations to create acid solutions, which were then added to a round-bottom flask.[45] Then, 250 mg of precisely weighed single-walled carbon nanotubes (SWCNT) were added to the acid solution as received. Next, a hot plate with a temperature setting of 120 °C was placed underneath and used to heat the round-bottom flask. It included a 5-hour refluxing phase that began as soon as the first reflux drops appeared. The process of acid refluxing was carried out while magnetic stirring was quite strong. After refluxing, the SWCNT solution was subjected to many dilutions and decantation cycles utilizing vacuum filtering and centrifugation. The SWCNTs solution was dried in an electric furnace for 24 hours at 80 °C once their pH had risen over 5. The dried functionalized single-walled carbon nanotubes (f-SWCNTs) were then crushed with a mortar and pestle into a powder.

2.5 Synthesis of silver citrate

For the synthesis of silver citrate, 1 g of $AgNO_3$ was dissolved in 50 mL DI water and stirred at 500 rpm at 100 °C. In a separate beaker, 0.5 g of $Na_3C_6H_5O_7$ and 3 g of NaOH were mixed in 30 mL DI water, and room temperature stirring was done at 500 rpm. The resulting solution was added dropwise to the $AgNO_3$ solution at a maintained stirring temperature of 100 °C for 10 minutes. Afterwards, the solution was placed in a centrifuge machine for centrifugation. Silver citrate precipitates were collected from the bottom of centrifuge tubes, and excess solvents were drained into the sink. Lastly, the silver citrate solution was dried for 12 hours at 110 °C in an oven. A comprehensive schematic illustrating the process of synthesizing silver citrate can be found in Fig. 1.

2.6 Synthesis of Ag/PANI/f-SWCNTs nanocomposite

The synthesis of an Ag/PANI/f-SWCNT nanocomposite, designated as Co, commenced with probe-sonication of 8 mg of f-SWCNTs in 30 mL of ethanol for 10 minutes. Subsequently, to achieve a targeted weight ratio of 3 : 1 : 1 for Ag/PANI/f-SWCNTs, 8 mg of PANI and 24 mg of silver citrate were added to the dispersed f-SWCNTs. Following that, a 10-minute probe-sonication of the whole solution was followed by a 12-hour drying process at 80 °C. This as-synthesized C_0 nanocomposite was then mixed in appropriate proportions with NiCoCu LDH to synthesize electrode materials. Fig. 1 shows a detailed schematic of the steps involved in producing C_0.

2.7 Preparation of electrodes

A 10.1 : 1 ratio of Ni–Co–Cu LDH (A_0, 5.45 mg) and Ag/PANI/SWCNTs (Co, 0.55 mg) nanocomposite was mixed manually. The electrode composition for electrochemical testing was an 80 : 10 : 10 mixture of active materials (A_0/C_0 nanocomposite), acetylene black, and an NMP-dissolved PVDF binder. In order to prepare the electrodes, the slurry was mixed extensively using a magnetic stirrer for a duration of 8 hours. The Ni-foam substrate was progressively washed for 10 minutes with acetone, ethanol, and HCl to get it ready for slurry deposition. Additionally, probe sonication was used to wash it with deionized (DI) water. Then, the mixture was uniformly deposited via drop-casting onto a 1 cm × 1 cm Ni-foam substrate acting as the current collector. The wet nickel foam was subsequently dried for ten hours at 80 °C. On the electrode, an estimated 6 mg of active mass was loaded. Similarly, two additional electrodes were fabricated for electrochemical analysis using the same process parameters. Different ratios of 10 : 1, 10 : 5, and 10 : 10, as shown in Table 1, for the active materials (Ni–Co–Cu LDH
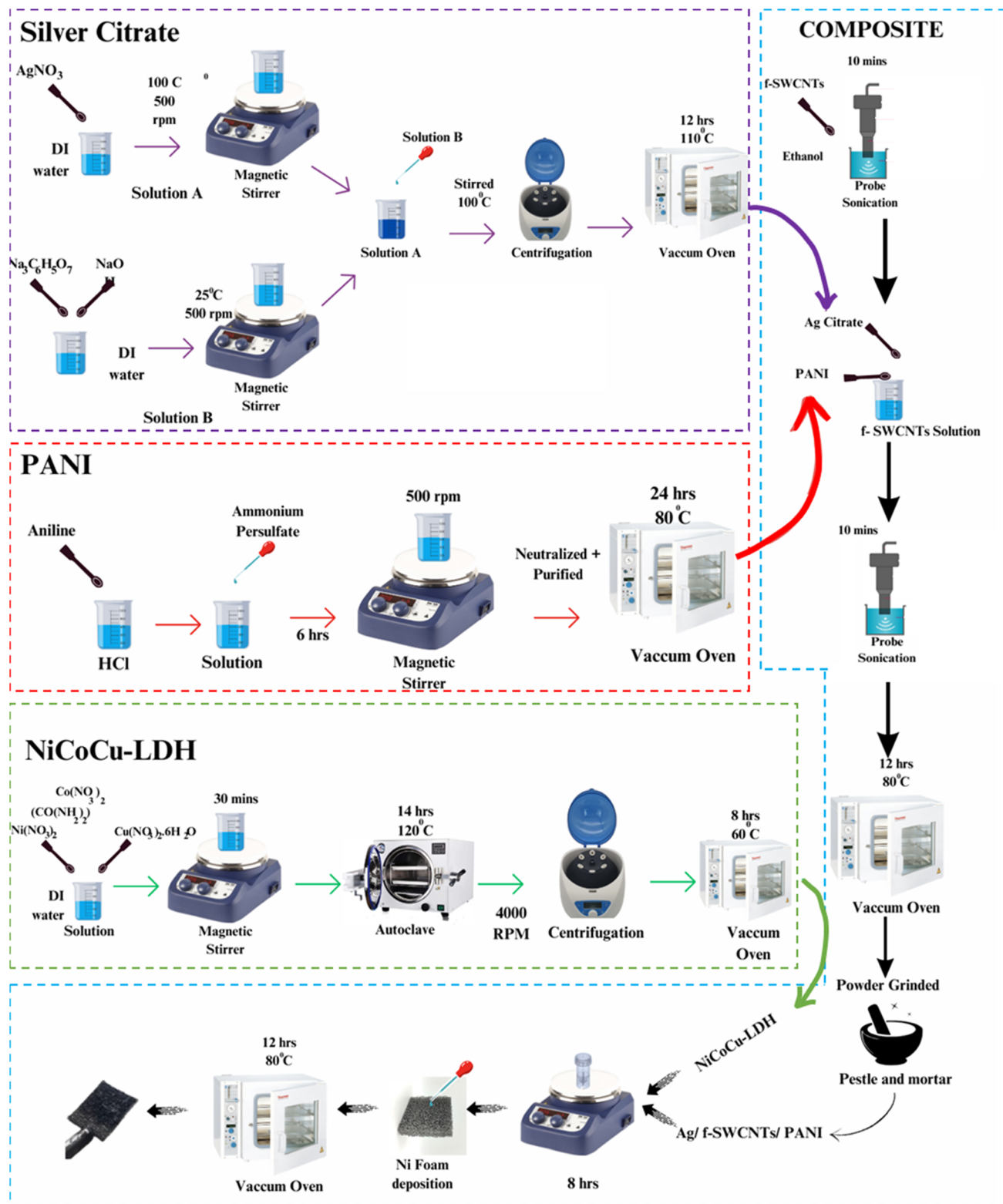
Fig. 1 (a) Shows a schematic of a 3 : 1 : 1 nanocomposite of C_0 (Ag/PANI/f-SWCNTs), A_0 (NiCoCu LDH), and electrode preparation.

and Co nanocomposite) and acetylene black were used, respectively, for electrode preparation. A comprehensive schematic illustrating the process of synthesizing electrode material can be found in Fig. 1.

2.8 Asymmetric supercapacitor device fabrication

Activated carbon (AC) was used as the negative electrode, and a NiCoCu LDH and Co nanocomposite were used as the positive

Table 1 List of prepared samples with amounts of active material added

Sample name	NiCoCu LDH (mg)	Ag/f-SWCNTs/PANI (mg)
A_0	6	0
A_1	5.45	0.55
A_2	4	2
A_3	3	3

electrodes to create the hybrid asymmetric supercapacitor (ASC) device. An electrolyte of potassium hydroxide (KOH) with 1 M concentration was used, and a Hoffman filter paper served as its separator. The negative electrode was prepared by combining AC, PVDF, and acetylene black at a mass ratio of $80:10:10$ in NMP solvent. This mixture was then applied to a 1 cm^2 porous Ni-foam piece using a micropipette. Subsequently, the slurry-coated Ni-foam was dried for eight hours at 80 °C in a vacuum oven.

2.9 Electrochemical analysis

The electrochemical testing of our material was conducted using a Gamry three-electrode assembly. In this assembly, our composites were the working electrodes: Pt wire as counter wire, and Hg/HgO was used as a reference electrode. 1 M of KOH solution in DI water was used as an electrolyte. A galvanostatic charge/discharge (GCD), cyclic voltammetry (CV), and electrochemical impedance spectroscopy (EIS) were used to evaluate the material's and the device's performance. A potentiostat (Galvanostat, Reference 3000, Gamry Instruments, USA) was utilized in testing electrodes and determining the cyclic stability of the device. Using the following formula shown in eqn (1), the specific capacitance, *i.e.*, C_s of the electrode, was determined from the cyclic voltammograms.

$$C_s = \frac{\int_{V_i}^{V_f} I \times \Delta V}{m \times v \times \Delta V} \quad (1)$$

here, V, measured in millivolts per second (mV s^{-1}), is the potential scan rate, m is the mass of the electrode material in grams, ΔV indicates the potential operating window, and C_s is the specific capacitance in farads per gram, and the area under the CV curve is specified by the integral function. The discharge curves can be used to calculate the specific capacity (Q_s) using the formula below.

$$Q_s = \frac{(I \times \Delta t)}{m} \quad (2)$$

where m is the electrode's mass, t is the discharge period, and I stands for the current density. The following equation was used to determine specific capacitance from GCD curves using eqn (2).

$$C_s = \frac{Q_s}{\Delta V} \quad (3)$$

The following eqn (4) and (5), were used to calculate the device's energy and power densities in watt-hour per kilogram (W h kg^{-1}) and watt per kilogram (W kg^{-1}), represented by E and P, respectively.

$$E = \frac{C_s \times V^2}{3.6 \times 2} \quad (4)$$

$$P = \frac{3600 \times E}{\Delta t} \quad (5)$$

2.10 Characterization

Scanning electron microscopy (SEM) equipped with energy-dispersive X-ray spectroscopy (EDS) (EVO 15 equipment from ZEISS in the United Kingdom) was used to examine the surface morphologies and elemental composition of the as-prepared NiCoCu LDH and Co nanocomposite. An XRD LPD diffractometer from Proto, United Kingdom, was used to analyze structural properties by X-ray diffraction (XRD) analysis. The X-ray intensity *vs.* two theta (2θ) was obtained using Cu-Kα radiation ($\lambda = 1.5418$ nm), which covered a range of 10° to 80° for 2θ diffraction angle. For electrochemical analysis, a potentiostat (Galvanostat, Reference 3000, Gamry Instruments, United States) was utilized. During electrode testing, a three-electrode assembly containing a Hg/HgO reference electrode and a platinum (Pt) wire counter electrode was used. As previously mentioned, Ni-foam was used in the fabrication of the device and the working electrode.

3. Results and discussion

3.1 Microstructure analysis and crystallography

Fig. 2 displays the diffraction patterns of three distinct composites that have been prepared and analyzed. According to ref. 46 and 47, diffraction peaks correspond to the (006), (002), (101), (104), and (101) planes of NiCoCu LDH (A_0) can be seen in the first spectrum at diffraction angles of 21.17°, 26.47°, 33.5°, 35.4°, and 59.81°, respectively.[48] On the other hand, in accordance with ref. 49 and 50, the spectrum of C_0 shows distinctive peaks of silver citrate at 27.61°, 32.35°, 44.64° attributed to (111), (200) and (220) planes respectively,[51] the broad hump at 20.89°, 25.40°, corresponds to (020), (200) crystal planes of PANI,[52] and finally the diffraction peaks 26° and 44.64° corresponds to (002) and (100) crystal planes of f-SWCNT. The diminished intensity is attributed to functionalization of SWCNTs and also due to very small weight ratio in the C_0.[53] Notably, as reported in references, the modified composite A_2 also showed characteristic peaks at diffraction angles of 26.76°, 33.5° and 59.7° corresponding to (002), (101), and (104) planes A_0, and at diffraction angles 25.6°, 27.6°, 30.27°, 32.35° and 34.19° corresponding to (200), (111), (003), (200), and (031) diffraction planes of C_0. The absence of a few peaks is likely due to low crystallinity, amorphous nature, and instrumentation factors, as reported in several studies.[54,55]

FTIR spectroscopy was used to investigate the bonding in our SC material as shown in Fig. 3. In the A_0 and A_2 spectra, we
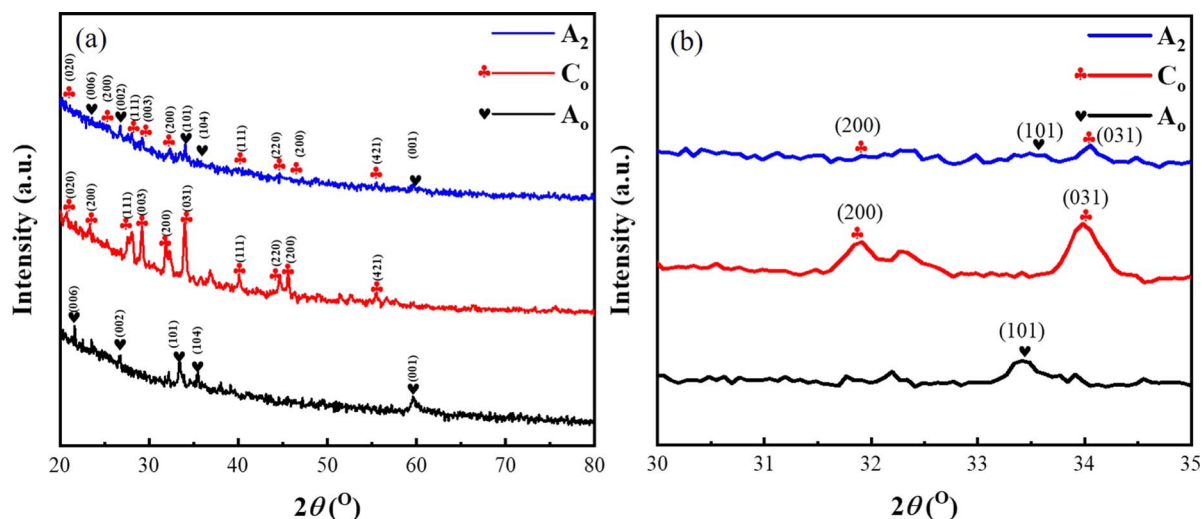
Fig. 2 The XRD analyses of the A_0, C_0, and A_2 electrodes throughout a 2θ diffraction angle range of (a) 20° to 80° and (b) 30° to 35°.
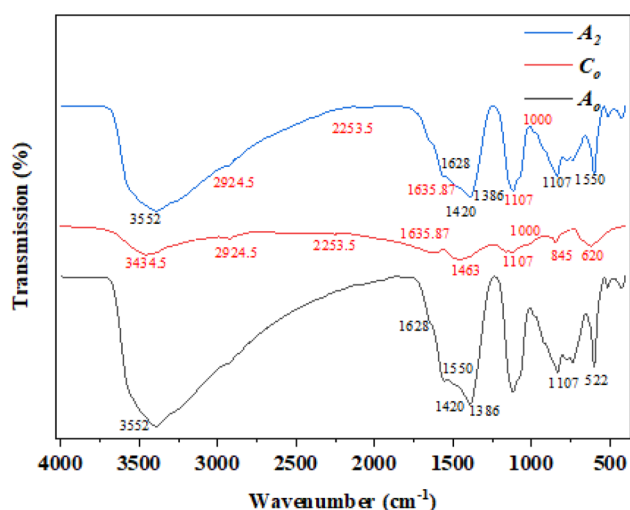

Fig. 3 The FTIR analyses spectra of the A_0, C_0, and A_2 electrodes throughout a wavenumber range of 500–5000 cm^{-1}.

discovered broad bands at 3552 and 1420 cm^{-1} wavenumbers are associated with bond vibration from alcohol hydroxyl groups.[48] While bands located at low frequencies *i.e.* 783, 605, 519, and 515 cm^{-1} are associated with the stretching of M–O vibrations, where M represents Ni, Cu, or Co.[48] The bands at 1463 and 1635 cm^{-1} in the FTIR spectra of C_0 are because of C–C stretching of benzenoid and quinonoid rings while bands at 1107 and 1000 cm^{-1} represents C–N stretching of benzenoid and quinonoid rings of pure PANI. Furthermore, bands at 2924 cm^{-1} shows O–H bond vibrations of carboxylic acid class, and C=O vibration at 1635 cm^{-1} was observed because of the presence of functionalization SWCNTs. In FTIR spectra of A_2, all M–O bonds along with hydrogen bonding O–H bands of alcohol were observed, indicating NiCoCu LDH. Moreover, bands at 2924 and 1635 cm^{-1} are due to the carboxylic acid O–H bond and C=O vibrations because of functionalized CNTs, while

widely spread band at 3552 cm^{-1} indicate the overlapping due to N–H, O–H vibrations, thus conforming with the expected composition of A_2.

Scanning Electron Microscopy (SEM) micrographs and the Energy Dispersive Spectroscopy's (EDS) elemental area mapping of the A_0 are displayed in Fig. 4(a), (b) and (c1)–(c3). At low magnification, a uniformly distributed cluster of nanoflakes with a lateral size of 0.5–1 μm can be seen in Fig. 4(a), which corresponds to a typical layered double hydroxide microstructure. The image obtained at greater magnification, *i.e.*, Fig. 4(b), reveals that the NiCoCu LDH nanoflakes are highly nanocrystallized with thickness in nanomaterial (<100 nm). The nickel (Ni), cobalt (Co), and copper (Cu) elements are uniformly distributed throughout the A_0 material, as confirmed by the EDS elemental area mapping of the A_0 sample, see Fig. 4(c1)–(c3); even dispersion of microstructure ascertains structure's strengthened compositional integrity. Fig. 4(d) and (e) clearly demonstrate the unique two-dimensional, plate-like structure of Ag citrate through A_2 SEM images, thin tubular structures of f-SWCNTs, and aggregates of PANI. A combination of Ag citrate nanosheet-like structure covered with aggregates of amorphous structure of PANI and 1D tubular structures confirms the nanocomposite formation. The EDS area mapping of the C_0 sample is shown in Fig. 4(f1)–(f3), which shows an equitable distribution of silver (Ag), carbon (C), and nitrogen (N). Similarly, Fig. 4(g) and (h) show the SEM analysis of A_2, which shows the presence of NiCoCu LDH nanoflakes and Ag citrate nanoplates covered with particles of PANI and 1D tubular structure of f-SWCNTs. EDS elemental maps shown in Fig. 4(i1)–(i6) confirm the presence of Ni, Co and Cu from A_0 and Ag, C, and N from C_0, thus confirming the physical bonding of LDH with nanocomposite.

3.2 Electrochemical analysis of three electrode assembly

3.2.1 CV analysis. Using a three-electrode arrangement, cyclic voltammetry (CV) is carried out on A_0 and its composites
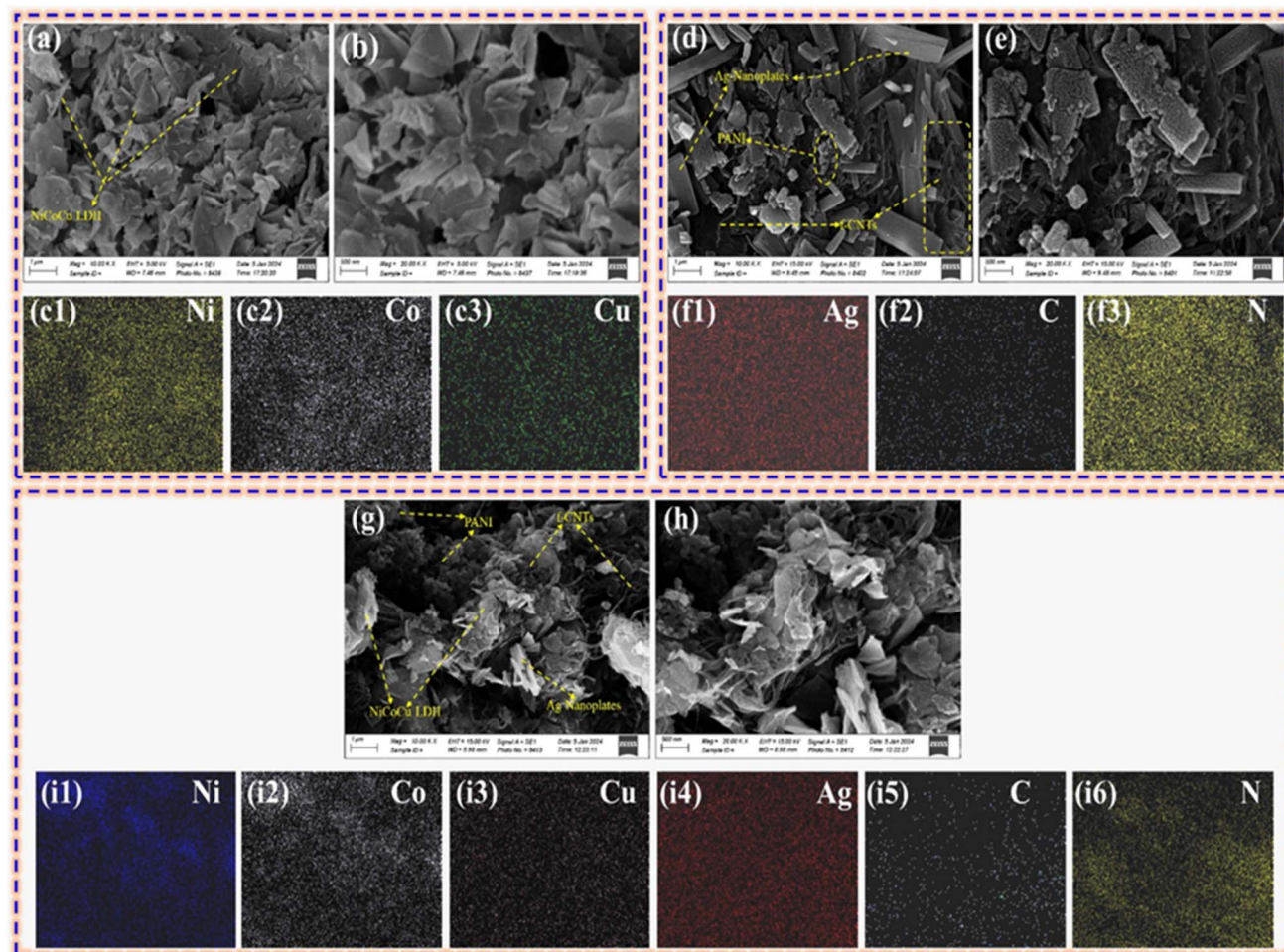
Fig. 4 SEM images of (a) A_0 (low magnification) (b) A_0 (high magnification) (d) C_0 (low magnification) (e) C_0 (high magnification) (g) A_2 (low magnification) (h) A_2 (high magnification) EDS elemental maps of (c1)–(c3) A_0 (f1)–(f3) C_0 (i1)–(i6) A_2.

A_1, A_2, and A_3 see Fig. 5(a)–(d). The electrolyte used contained a 1 M solution of KOH, and the voltage range was 0–0.7 V. A 2–50 mV s^{-1} range was used for the scan rate of CV analysis. The presence of redox peaks in the cyclic voltammetry (CV) curve of A_0 shown in Fig. 5(a) indicates the faradaic reaction and electrolyte ions. Faradaic processes governed by Faraday's law show redox peaks which are primarily linked to M–O/M–O–ON, where M denotes Ni, Co, or Cu ions and N denotes H or K ions,[56,57] suggesting that the generated electrode materials were pseudocapacitive, accompanied by a significantly smaller area under the curve, which suggests a less specific capacitance. The peak current increasing and specific capacitance (C_s) decreasing resulted from increasing the scanning rate from 2 to 50 mV s^{-1} is observed in all samples, which is due to insufficient time for electrolyte ions to interact with the electrode material. Furthermore, Fig. 5(b) displays a CV of A_1, which supports the synergistic effect of compositing with C_0. Though the voltammogram's shape slightly changes after the oxidation peak potential is reached, the CV curve's larger area under the curve than A_0 is indicative of a higher specific capacitance. Incorporating EDLC-type materials, such as SWCNTs, causes the peak to expand, indicating hybrid behaviour. Fig. 5(c), which shows

the voltammogram of the best-performing sample A_2, illustrates hybrid behavior by showing a similar rise in redox peak spread due to the larger weight percent of C_0. Weight percent ratio optimization for pristine and C_0 is supported by the largest integrated area under the curve of A_2 out of all samples, indicating enhanced C_s. The voltammogram of A_3, as seen in Fig. 5(d), shows that peak broadening persists with additional C_0 increment, indicating the retention of hybrid behavior. However, the integrated area of the CV curve decreased, indicating a lower C_s in comparison to A_2, presumably as a result of a reduced surface area from the agglomeration of composite material.[58]

3.2.2 GCD analysis. To examine the charge–discharge process behavior, GCD analysis was carried out for each of the four electrodes; Fig. 6(a)–(d) shows the results. Fig. 6(a) shows the discharging profile of A_0 with a voltage potential window from 0 V to 0.5 V. The discharging duration of A_0 is plotted *versus* potential (V *vs.* Hg/HgO) at various current densities spanned from 0.5 A g^{-1} to 6 A g^{-1}. As we increased the current density from 0.5 A g^{-1} to 6 A g^{-1}. The reduction in discharging time as the current density increases is related to the limited ion diffusion rate, which is a commonly observed phenomenon in
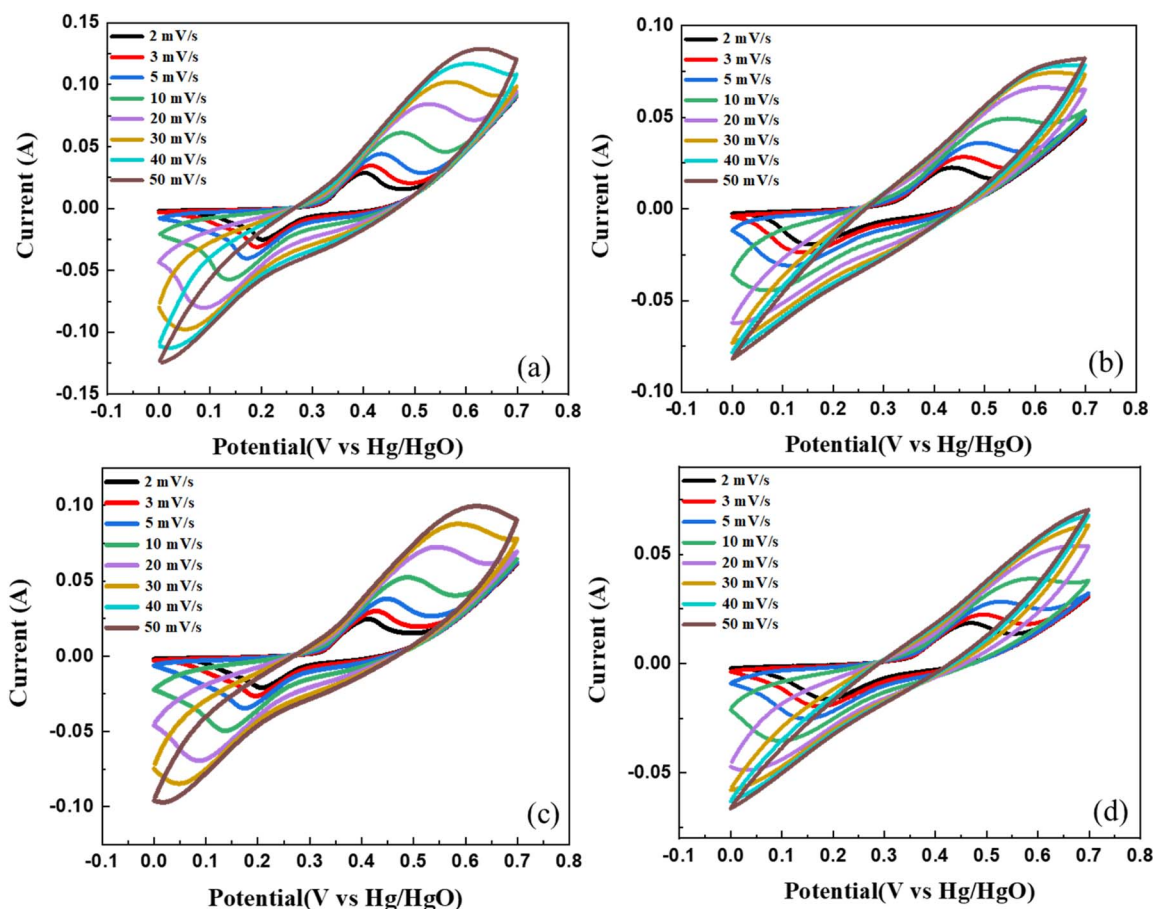
Fig. 5 Cyclic voltammogram of various samples, *i.e.*, (a) A_0, (b) A_1, (c) A_2, and (d) A_3 at scan rates of 2–50 mV s^{-1}.

energy storage devices. As the current density rises, the rate at which ions can move to and from the electrodes becomes constrained, leading to shorter discharging durations. Therefore, during the redox process, charge storage is limited to the outer active surface of the electrode material. It is important to note that the A_0 (LDH) electrode displays a total discharge duration of 422 seconds. Additionally, Fig. 6(b)–(d) exhibit the discharging curves corresponding to varying weight percentages of Ag/f-SWCNTs/PANI added to NiCoCu LDH, as previously abbreviated: A_1, A_2, and A_3. A_1 and A_3 had discharge times of 656 and 616 seconds, respectively, at 0.5 A g^{-1} of current density, whereas the composite of interest, A_2, showed the highest discharging duration of around 807 seconds.

3.2.3 Comparison analysis. Fig. 7(a) displays the CV comparison curve for A_0, A_1, A_2, and A_3 at 10 mV s^{-1}. With C_0 added (until 10:5), the performance of the composites increased; A_2 had the largest integrated area under the CV curve (10 mV s^{-1}) denoting highest specific capacitance as shown in Fig. S1 of the ESI.† From GCD analysis we realized that as the proportion of C_0 rose above 10:5, the composite's performance began to decline. The nonlinearity in the discharging curves of the A_0, A_1, A_2, and A_3 (see Fig. 7(b)), which show conventional hybrid characteristics exhibiting both faradaic and non-faradaic processes, provide strong support for the conclusions made in

explaining CV curves. For the same current density of 0.5 A g^{-1}, the A_2 composite shows a longer discharge time than A_0, A_1, and A_3, indicating superior charge storage performance. The observed extension in discharge time can be ascribed to the optimal presence of composite materials, likely by the enhanced conductivity and ion diffusion up to a specific concentration. However, with a subsequent increase in composite material, the discharge time diminished, presumably due to agglomeration.[59]

The effect of C_0 addition on the electrochemical behavior of A_0 was investigated further using electrochemical impedance spectroscopy (EIS), improved charge transfer kinetics in electrodes was observed across the board. The Nyquist plots of the electrodes A_0, A_1, A_2, and A_3 are shown in Fig. 7(c) and S2 of the ESI,† where the high-frequency zone is represented by arcs and the low-frequency region by linear forms. The curve at high frequency represents the contact resistance of the electrode, the ionic resistance of the electrolyte, and the internal resistance of the active material. Higher capacitance retention is a result of rapid electron transfer caused by A_2's low R_{ct}. According to this result, there are more conductive transmission pathways available for electron transport when C_0 is added. Warburg impedance (W), represented by the slope in the low-frequency zone, shows capacitance properties having lower values for A_2 than A_1,
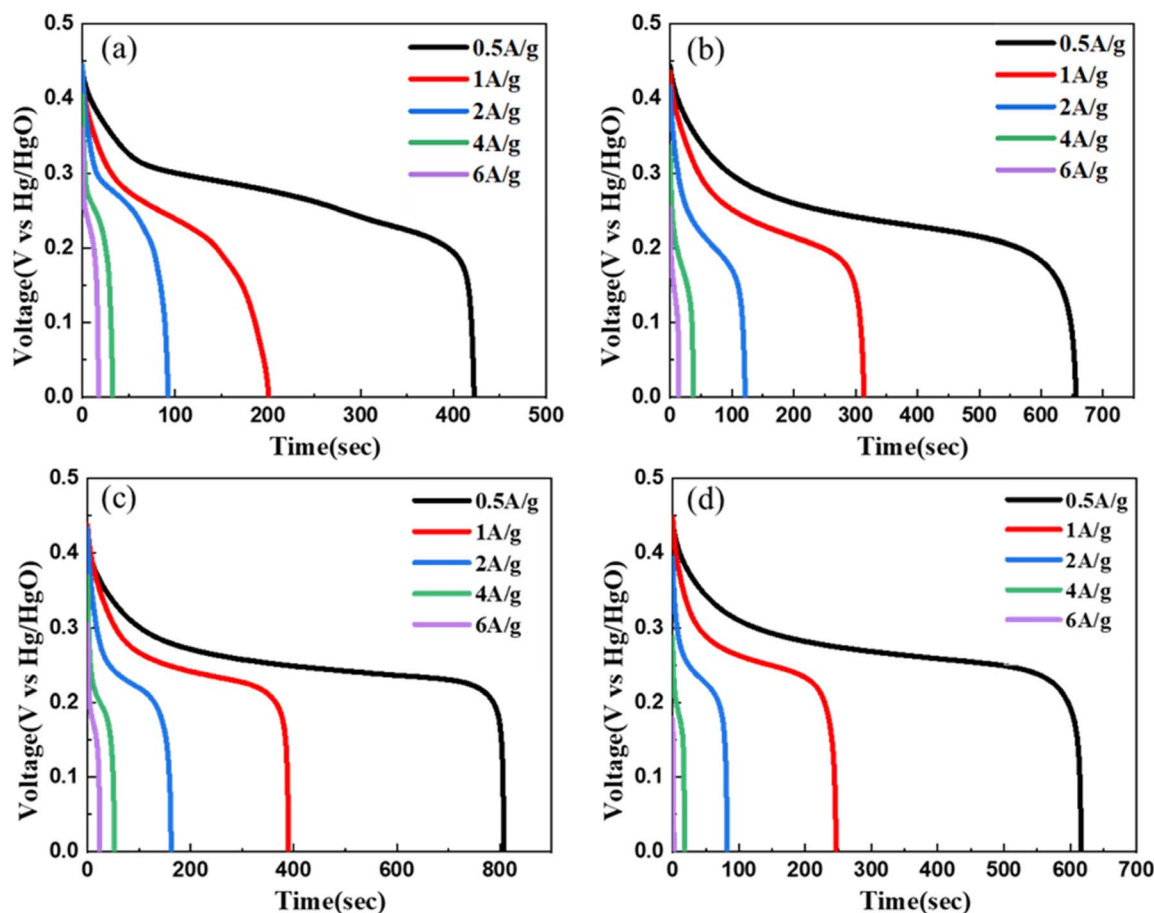
Fig. 6 GCD analysis discharge curves at potential window of 0.5 V of (a) A_0, (b) A_1, (c) A_2 and (d) A_3 at current densities from 0.5 A g^{-1} to 6 A g^{-1}.

and A_3. EIS fitted values, *i.e.*, R_s, R_{ct}, and W for three electrodes, are shown in Table 2.

The A_2 composite exhibits the highest specific capacitances of the three electrodes, as shown in Fig. 8, and has the longest discharge time, indicating superior charge storage performance. The peak capacitance of A_2 is 807 F g^{-1} (at 0.5 A g^{-1}), as derived from eqn (3). In addition, as shown in Fig. S1 of the ESI,† the specific capacitance derived from CV curves using eqn (1) shows a similar trend, *i.e.*, comparably higher specific capacitance for the A_2 sample. The specific capacitance of an electrode material decreases gradually due to the limited time available for electrolytic ions to diffuse throughout the electrode structure. Notably, even beneath high current densities (300 F g^{-1} at 6 A g^{-1}), the electrodes, especially A_2, maintained their specific capacitance and demonstrated superior performance overall, highlighting its exceptional capacitance retention. Table 3 further distinctly delineates the significance of the present study, as the specific
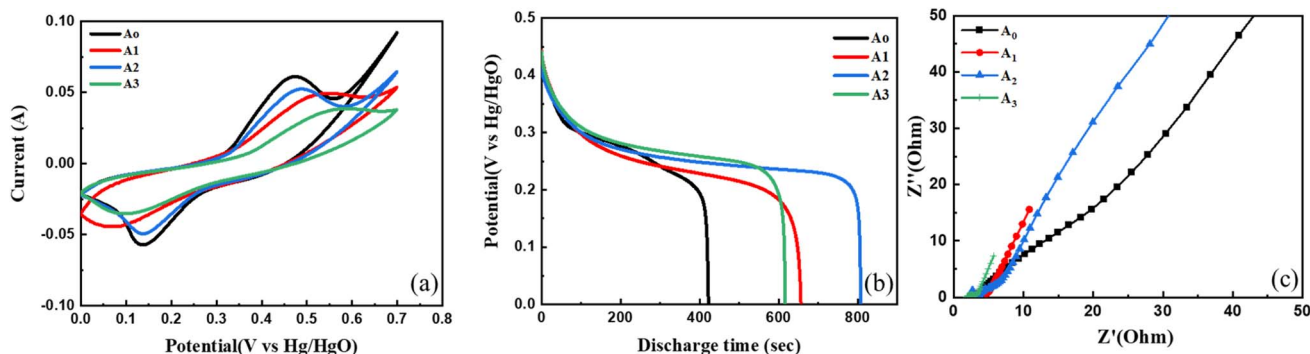

Fig. 7 (a) Cyclic voltammograms at a specified scan rate, *i.e.*, 10 mV s^{-1}, (b) discharge curves at a specified current density, *i.e.*, 0.5 A g^{-1}, and (c) Nyquist plots of A_0 and its composites A_1, A_2, and A_3.

Table 2 Pristine and composite electrodes with varying resistance values (of R_s, R_{ct}, and W), using an EIS-fitted solution

Electrode materials	R_s (ohms)	R_{ct} (ohms)	W (ohms)
A_0	0.00009	3.502	0.00019
A_1	0.92630	3.807	0.06183
A_2	2.508	3.422	0.006
A_3	1.51100	1.802	0.02566
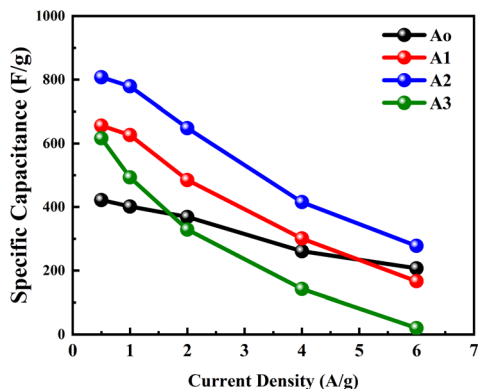
Fig. 8 Comparison of specific capacitance for pristine and composites.

capacitance attained surpasses that of other documented research efforts.

3.3 Electrochemical analysis of asymmetric supercapacitor device

3.3.1 CV and GCD analysis. To evaluate the electrochemical performance of A_2 in practical applications, an asymmetric device was made using A_2 as positive electrode material and AC as negative material partitioned by filter paper dipped in a KOH solution (1 M). Electrochemical studies such as GCD, CV, and EIS were conducted. For the AC electrode, CV was performed using alternating current in the potential range of 0 to -1 V, resulting in a rectangular cyclic voltammogram, which indicates the behavior of a double-layer capacitance. Conversely, Fig. 9(a) illustrates that the A_2 electrode's cyclic voltammogram clearly displayed redox peaks between 0 and 0.7 V, indicating a hybrid behavior. A series of cyclic voltammetry (CV) curves was obtained at a scan rate of 30 mV s^{-1} under different potential windows to determine the optimal operating voltage for the

$A_2\|AC$ device. The stable electrochemical performance of the device can be extended to 1.7 V, suggesting that the assembled system has real world application potential as shown in Fig. 9(b). This allowed for the assessment of the optimal working voltage. Hence, a potential window of 0 V to 1.7 V was used for scan rates varying from 3 mV s^{-1} to 100 mV s^{-1}, shown in Fig. 9(c). The CV curve of AC$\|A_2$ shows a consistent quasi-rectangular profile at varying scan rates, which indicates a hybrid charge storage mechanism. This indicates that there are quick and reversible charge storage processes linked with EDLC. However, any changes or sloping areas in the curve at increased scan rates could suggest the involvement of pseudo-capacitance from redox reactions or surface-bound charge storage processes.[65] The retention of the CV (see Fig. 9(c)), as well as GCD curves (see Fig. S3 in ESI†) at varying scan rates and potential windows, respectively, ascertain high reversibility and exceptional overall electrochemical performance of our asymmetric device by storing and delivering energy reliably over multiple charging and discharging cycles.[66] Fig. 9(d) shows the GCD analysis of the AC$\|A_2$ device at different current densities varying from 1.5 A g^{-1} to 14 A g^{-1} using a potential window of 1.7 V. The discharge time at 1.5 A g^{-1} was used to calculate the energy density and power density of the AC$\|A_2$ device using eqn (4) and (5); calculations revealed 62.15 W h kg^{-1} energy density and 1275 W kg^{-1} power density at a current density of 1.5 A g^{-1}. At 14 A g^{-1}, it showed 22.44 W h kg^{-1} of energy density and 11 900 W kg^{-1} of power density.

3.3.2 Specific capacitance, Ragone plot, stability, and impedance analysis. Fig. 10(a) demonstrates the $A_2\|AC$ device's specific capacitance trend as determined by spanning current densities from 1.5 A g^{-1} to 14 A g^{-1}. Fig. 10(b) indicates the Ragone plot depicting the power and energy density values at various current densities. To assess the practical performance of the ASC device, it was charged and discharged for 4000 cycles at a current density of 14 A g^{-1}, which showed cyclic stability of up to 100% and coulombic efficiency of up to 95% as shown in Fig. 10(c). The Nyquist plots for the built device, displaying the EIS spectra of the first (before) and after life cycle test, are shown in Fig. S4(a) and (b) in the ESI.† As anticipated, the device showed a straight line in the low-frequency zone which represents the Warburg diffusion element, reflecting the diffusion-limited processes. On the other hand, a semicircle in the high-frequency region corresponds to the charge transfer resistance. The semicircle diameter measurements indicated a brief path traveled by an electron or ion due to the low cell resistance prior to cycling. The longer ion/electron transport

Table 3 Shows the comparison of current research in light of previous works

| Materials	Method of synthesis	Specific capacitance	Electrolyte	Ref.
3D Co–Al-LDHs	Hydrothermal	801@5 A g^{-1}	2 M KOH	60
CNTs/CoNiFe-LDH	Hydrothermal	170.6@1 A g^{-1}	6 M KOH	61
NPCs-2-700	Carbonization/activation	341@1 A g^{-1}	6 M KOH	62
Ce doped NiCo-LDH/CNT	Hydrothermal	187.2@1 A g^{-1}	1 M KOH	63
CoFe-LDH@ZnO@CC	Hydrothermal	299.8@2 A g^{-1}	1 M Na$_2$SO$_4$	64
NiCoCu-LDH/CNT/PANI/Ag	Hydrothermal at 120 °C for 12 h	807 F g^{-1}@0.5 A g^{-1}	1 M KOH	This work
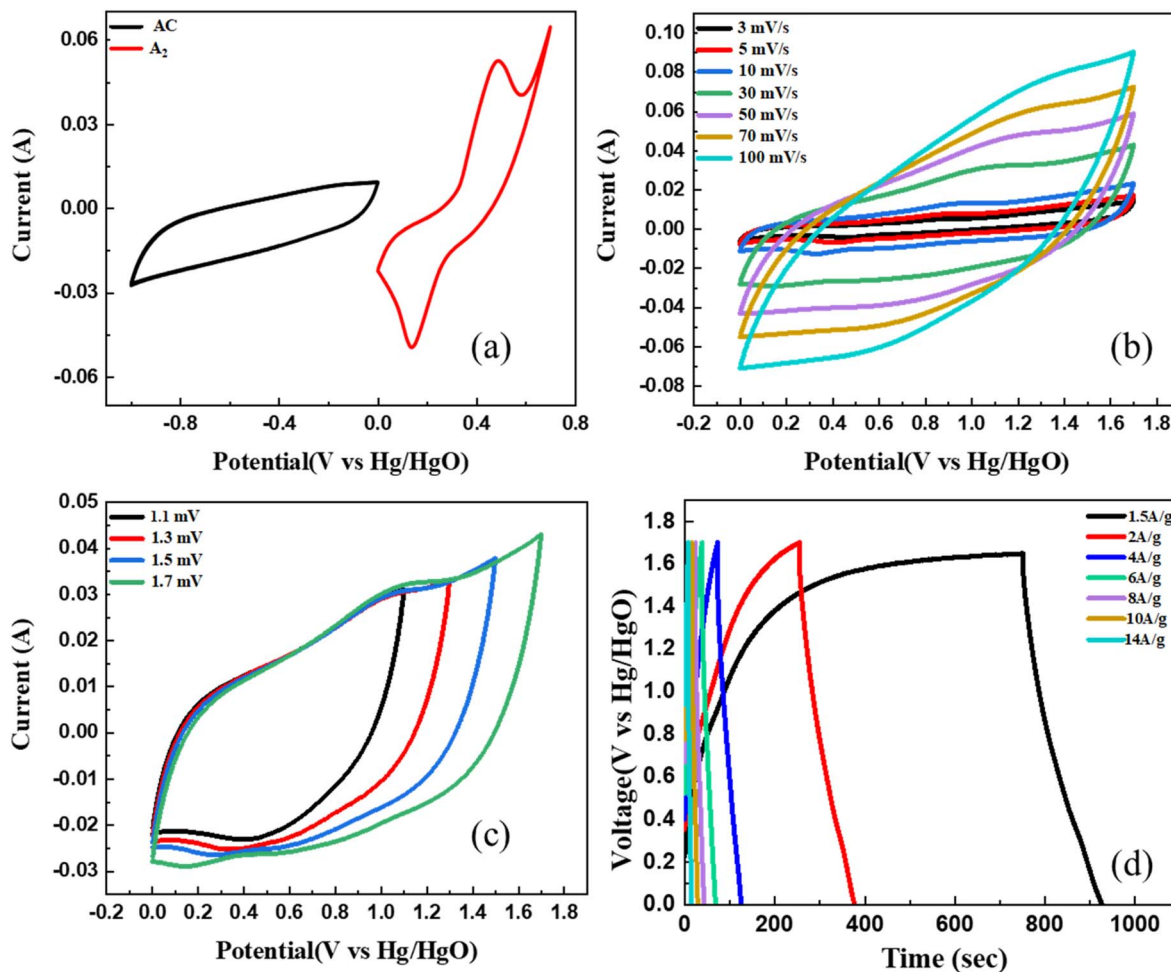
Fig. 9 Electrochemical analysis of A_2||AC ASC device (a) CV for activated carbon and A_2 at 10 mV s^{-1} scan rate (b) CV at different potential windows from 1.1 mV to 1.7 mV (c) CV at varying scan rates from 3 mV s^{-1} to 100 mV s^{-1} (d) GCD at varying current densities from 1.5 A g^{-1} to 14 A g^{-1}.

channel was later discovered by the EIS spectrum, as seen by the increased charge transfer resistance. Similarly, the Nyquist plot's high line gradient in the low-frequency zone prior to cycling indicated low interfacial diffusion resistance (rapid ion diffusion and mass transport at the electrode/electrolyte

interface).[67] As a result, the device's charge transfer resistance values were obtained from the Nyquist plots as $R_{ct} = 2.048\ \Omega$ (before) and $R_{ct} = 157.2\ \Omega$ (after).

3.3.3 Device's behavior analysis. The study of diffusive and capacitive behavior required the calculation of b-values from
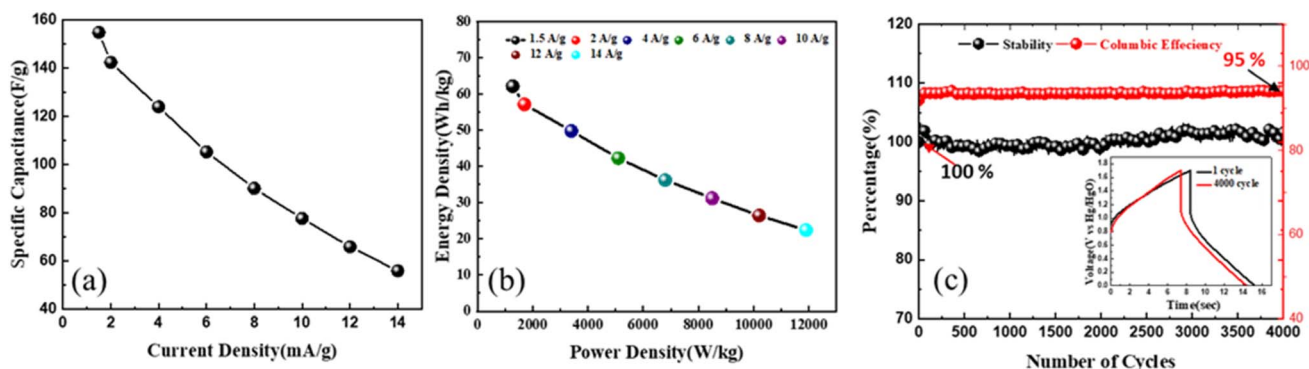

Fig. 10 (a) Specific capacitance at different current densities (b) Ragone plot (c) cyclic stability for 4000 cycles at a current density of 14 A g^{-1} of AC||A_2 device.
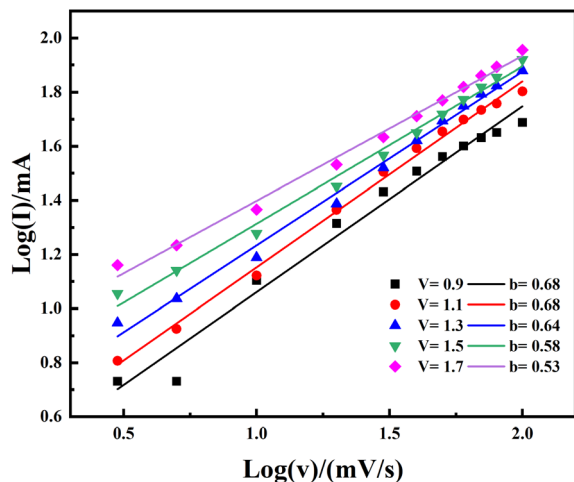
Fig. 11 The calculated *b*-values by fitting the logarithm of current (log(*i*)) linearly against the logarithm of voltage (log(*v*)) at different potentials.

the CV curves using the power law equation represented by eqn (6).

$$i = av^b \tag{6}$$

In the above equation, which represents the relationship between the electric current (*i*), scanning rate (*v*), and adjustable factors (*a* and *b*), the gradient value is represented by the symbol *b*. Applying a logarithmic transformation to both sides of the eqn (6) allows for the analysis of the relationship between *i* and *v*, which is beneficial for understanding underlying behavior through eqn (7)

$$\log(i) = \log(a) + b\log(v) \tag{7}$$

Parameter *b* spans three different intervals: (i) 1 denotes a supercapacitor; (ii) 0.5 denotes a battery-grade caliber material; and (iii) a value between 1 and 0.5 represents a mixed nature of the device. Fig. 11 provides a visual representation of the entire evaluation of *b* coefficients. Upon careful analysis, *b* coefficients are distributed between 0.5 and 1 (see Fig. 11). It emphasizes the simultaneous occurrence of both faradaic and non-faradaic responses, therefore capable of accommodating both high power delivery (supercapacitor-like behavior) and high energy density (battery-like behavior), hence attesting to a hybrid charge storage mechanism. The determined *b* coefficients substantiate our postulation of a coupled hybrid supercapacitor arrangement.

4.   Conclusion

In conclusion, the integration of layered double hydroxides (LDH) and highly conductive materials has shown significant promise in bridging the energy and power density disparities within energy storage technologies. Through the synthesis and evaluation of four distinct electrodes, this study has demonstrated the exceptional electrochemical properties of the

optimal electrode, through specific design and composition, allowing for improved charge storage capabilities and overall efficiency in supercapacitor applications, notably achieving specific capacitances of 807 F g⁻¹ at 0.5 A g⁻¹, twice as high as those of pure samples. The assembled A₂/AC ASC device showcased impressive energy densities of 62.15 W h kg⁻¹ and 22.44 W h kg⁻¹, corresponding to power densities of 11 900 W kg⁻¹ and 1275 W kg⁻¹, respectively, while maintaining high coulombic efficiency of 95% and operational capacity over four thousand cycles. The characterization of the power law further supports the proposition of a hybrid-grade supercapacitor, with *b*-values falling in the range of 0.5 to 1.

Data availability

The data that support the findings of this study are available from the corresponding author upon reasonable request.

Conflicts of interest

There are no conflicts to declare.

References

1 S. Bi, H. Banda, M. Chen, L. Niu, M. Chen, T. Wu, J. Wang, R. Wang, J. Feng, T. Chen, M. Dincă, A. A. Kornyshev and G. Feng, *Nat. Mater.*, 2020, **19**, 552–558.
2 C. Choi, D. S. Ashby, D. M. Butts, R. H. DeBlock, Q. Wei, J. Lau and B. Dunn, *Nat. Rev. Mater.*, 2020, **5**, 5–19.
3 Z. Li, S. Gadipelli, H. Li, C. A. Howard, D. J. L. Brett, P. R. Shearing, Z. Guo, I. P. Parkin and F. Li, *Nat. Energy*, 2020, **5**, 160–168.
4 P. Simon and Y. Gogotsi, *Nat. Mater.*, 2020, **19**, 1151–1163.
5 Q. Wu, T. He, Y. Zhang, J. Zhang, Z. Wang, Y. Liu, L. Zhao, Y. Wu and F. Ran, *J. Mater. Chem. A*, 2021, **9**, 24094–24147.
6 X. Zhang, C. Jiang, J. Liang and W. Wu, *J. Mater. Chem. A*, 2021, **9**, 8099–8128.
7 Y. Zhao, H. Li, R. Tang, X. Wang, Y. Wu, S. Yan and Y. Zhang, *J. Mater. Chem. A*, 2023, **11**, 15844–15854.
8 A. Inman, T. Hryhorchuk, L. Bi, R. Wang, B. Greenspan, T. Tabb, E. M. Gallo, A. VahidMohammadi, G. Dion, A. Danielescu and Y. Gogotsi, *J. Mater. Chem. A*, 2023, **11**, 3514–3523.
9 T. A. Gaber, L. R. Ahmed and A. F. M. El-Mahdy, *J. Mater. Chem. A*, 2023, **11**, 19408–19417.
10 J. M. Lim, Y. S. Jang, H. V. T. Nguyen, J. S. Kim, Y. Yoon, B. J. Park, D. H. Seo, K.-K. Lee, Z. Han, K. Ostrikov and S. G. Doo, *Nanoscale Adv.*, 2023, **5**, 615–626.

11 S. Ansari, R. B. Choudhary and A. Gupta, *J. Energy Storage*, 2023, **59**, 106446.

12 X. Wei, B. Qiu, H. Tian, Y. Lv, W. Zhang, Q. Qin, Z. Liu and F. Wei, *Appl. Surf. Sci.*, 2023, **615**, 156280.

13 Y. K. Sonia and S. K. Meher, *Sustainable Energy Fuels*, 2023, 7, 2895–2909.

14 S. Mahala, K. Khosravinia and A. Kiani, *J. Energy Storage*, 2023, **67**, 107558.

15 J. Ahn, Y. Song, Y. J. Kim, D. Nam, T. Kim, K. Kwak, C. Hoon Kwon, Y. Ko, S. J. Lee and J. Cho, *Chem. Eng. J.*, 2023, **455**, 140742.

16 M. Ashtar, M. A. Marwat, Y. X. Gao, Z. T. Zhang, L. Pi, S. L. Yuan and Z. M. Tian, *J. Mater. Chem. C*, 2019, 7, 10073–10081.

17 M. Fawad Khan, M. Ali Marwat, Abdullah, S. Shaheen Shah, M. R. Abdul Karim, M. Abdul Aziz, Z. Ud Din, A. Saad and K. Muhammad Adam, *Sep. Purif. Technol.*, 2023, **310**, 123101.

18 K. M. Adam, M. A. Marwat, M. F. Khan, M. Humayun, S. S. Shah, Z. U. Din, M. R. A. Karim, M. Bououdina, S. Abdullah and E. Ghazanfar, *J. Energy Storage*, 2024, **81**, 110448.

19 S. Ali, M. A. Marwat, M. F. Khan, K. M. Adam, Z. U. Din, M. R. A. Karim and S. Khan, *J. Alloys Compd.*, 2023, **956**, 170229.

20 S.-J. Shin, J. W. Gittins, C. J. Balhatchet, A. Walsh and A. C. Forse, *Adv. Funct. Mater.*, 2023, 2308497.

21 A. Zhang, Q. Zhang, H. Fu, H. Zong and H. Guo, *Small*, 2023, **19**, 2303911.

22 M. A. Marwat, S. Ishfaq, K. M. Adam, B. Tahir, M. H. Shaikh, M. F. Khan, M. R. Abdul Karim, Z. U. Din, S. Abdullah and E. Ghazanfar, *RSC Adv.*, 2024, **14**, 2102–2115.

23 P. K. Ray, R. Mohanty and K. Parida, *J. Energy Storage*, 2023, **72**, 108335.

24 S. Alam, M. I. K. F. Fiaz, M. Z. Iqbal, F. Alam, Z. Ahmad and H. H. Hegazy, *J. Energy Storage*, 2023, **72**, 108208.

25 J. Zhao, J. Chen, S. Xu, M. Shao, D. Yan, M. Wei, D. G. Evans and X. Duan, *J. Mater. Chem. A*, 2013, **1**, 8836–8843.

26 M. E. Spahr, P. Novák, B. Schnyder, O. Haas and R. Nesper, *J. Electrochem. Soc.*, 1998, **145**, 1113.

27 J. Han, Y. Dou, J. Zhao, M. Wei, D. G. Evans and X. Duan, *Small*, 2013, **9**, 98–106.

28 Y. Tao, L. Zaijun, L. Ruiyi, N. Qi, K. Hui, N. Yulian and L. Junkang, *J. Mater. Chem.*, 2012, **22**, 23587–23592.

29 Y. Cheng, H. Zhang, C. V. Varanasi and J. Liu, *Energy Environ. Sci.*, 2013, **6**, 3314–3321.

30 Z. Chen, H. Deng, M. Zhang, Z. Yang, D. Hu, Y. Wang and K. Yan, *Nanoscale Adv.*, 2020, **2**, 2099–2105.

31 Z. Lu, Z. Chang, W. Zhu and X. Sun, *Chem. Commun.*, 2011, **47**, 9651–9653.

32 H. Chen, J. Jiang, Y. Zhao, L. Zhang, D. Guo and D. Xia, *J. Mater. Chem. A*, 2015, **3**, 428–437.

33 F. Wang, S. Sun, Y. Xu, T. Wang, R. Yu and H. Li, *Sci. Rep.*, 2017, 7, 4707.

34 S. C. Sekhar, G. Nagaraju and J. S. Yu, *Nano Energy*, 2017, 58–67.

35 J. Yang, C. Yu, X. Fan, Z. Ling, J. Qiu and Y. Gogotsi, *Mater. Chem. A*, 2013, 1963–1968.

36 S. Ramandi and M. H. Entezari, *J. Energy Storage*, 2022, 106106.

37 X. Li, D. Du, Y. Zhang, W. Xing, Q. Xue and Z. Yan, *J. Mater. Chem. A*, 2017, **5**, 15460–15485.

38 J. Wang, D. Jiang, M. Zhang, Y. Sun, M. Jiang, Y. Du and J. Liu, *J. Mater. Chem. A*, 2023, **11**, 1419–1429.

39 F. Ahmad, M. Zahid, H. Jamil, M. A. Khan, S. Atiq, M. Bibi, K. Shahbaz, M. Adnan, M. Danish and F. Rasheed, *J. Energy Storage*, 2023, **72**, 108731.

40 Q. Xu, X. Liu, J. Zhang, Y. Xu, M. Zhou, J. Li, M. Du, K. Zhang, X. Qian and B. Xu, *J. Mater. Chem. A*, 2023, **11**, 5309–5319.

41 S. R. KA, K. Pramoda and C. S. Rout, *J. Mater. Chem. C*, 2023, **11**, 2565–2573.

42 B. Shen, X. Liao, X. Hu, H.-T. Ren, J.-H. Lin, C.-W. Lou and T.-T. Li, *J. Mater. Chem. A*, 2023, **11**, 16823–16837.

43 G. S. R. Raju, S. Kondrat, N. R. Chodankar, S.-K. Hwang, J. H. Lee, T. Long, E. Pavitra, S. J. Patil, K. S. Ranjith and M. B. Rao, *J. Mater. Chem. A*, 2023, **11**, 15540–15552.

44 M. A. Marwat, S. Ishfaq, K. M. Adam, B. Tahir, M. H. Shaikh, M. F. Khan, M. R. A. Karim, Z. U. Din, S. Abdullah and E. Ghazanfar, *RSC Adv.*, 2024, **14**, 2102–2115.

45 N. Sezer and M. Koç, *Surf. Interfaces*, 2019, **14**, 1–8.

46 R. Ramachandran, Y. Lan, Z.-X. Xu and F. Wang, *ACS Appl. Energy Mater.*, 2020, **3**, 6633–6643.

47 L. Zhou, Y. He, Y. Jia, V. Pavlinek, P. Saha and Q. Cheng, *Nanomaterials*, 2017, 7, 273.

48 A. Raja, N. Son, Y.-I. Kim and M. Kang, *J. Colloid Interface Sci.*, 2023, **647**, 104–114.

49 W. Yang, C. Wang and V. Arrighi, *J. Mater. Sci.: Mater. Electron.*, 2018, **29**, 2771–2783.

50 Z. Hu, C. Kong, Y. Han, H. Zhao, Y. Yang and H. Wu, *Mater. Lett.*, 2007, **61**, 3931–3934.

51 M. Govindappa, H. Farheen, C. P. Chandrappa, Channabasava, R. V. Rai and V. B. Raghavendra, *Adv. Nat. Sci.: Nanosci. Nanotechnol.*, 2016, 7, 035014.

52 S. P. Deshmukh, A. G. Dhodamani, S. M. Patil, S. B. Mullani, K. V. More and S. D. Delekar, *ACS Omega*, 2020, **5**, 219–227.

53 M.-S. Park, K. H. Kim and Y.-S. Lee, *J. Ind. Eng. Chem.*, 2016, **37**, 22–26.

54 P. M. A. Sherwood, in *Encyclopedia of Materials: Science and Technology*, ed. K. H. J. Buschow, R. W. Cahn, M. C. Flemings, B. Ilschner, E. J. Kramer, S. Mahajan and P. Veyssière, Elsevier, Oxford, 2001, pp. 985–995, DOI: **10.1016/B0-08-043152-6/00183-2**.

55 W. Stillwell, in *An Introduction to Biological Membranes*, ed. W. Stillwell, Elsevier, 2nd edn, 2016, pp. 135–180, DOI: **10.1016/B978-0-444-63772-7.00009-9**.

56 U. M. Patil, K. V. Gurav, V. J. Fulari, C. D. Lokhande and O. S. Joo, *J. Power Sources*, 2009, **188**, 338–342.

57 J. Wang, Q. Ding, C. Bai, F. Wang, S. Sun, Y. Xu and H. Li, *Nanomaterials*, 2021, **11**, 2155.

58 D.-G. Jeung, M. Lee, S.-M. Paek and J.-M. Oh, *Nanomaterials*, 2021, **11**, 455.

59 B. Arumugam, G. Mayakrishnan, S. K. Subburayan Manickavasagam, S. C. Kim and R. Vanaraj, *Crystals*, 2023, **13**, 1118.

60 J. Zai, Y. Liu, X. Li, Z.-f. Ma, R. Qi and X. Qian, *Nano-Micro Lett.*, 2016, **9**, 21.

61 J. Wang, Q. Ding, C. Bai, F. Wang, S. Sun, Y. Xu and H. Li, *Nanomaterials*, 2021, **11**, 2155.

62 J. Yu, N. Fu, J. Zhao, R. Liu, F. Li, Y. Du and Z. Yang, *ACS Omega*, 2019, **4**, 15904–15911.

63 M. Dinari, H. Allami and M. M. Momeni, *Energy Fuels*, 2021, **35**, 1831–1841.

64 A. Mateen, M. Zubair, M. Saleem, A. Golubenkova, L. Voskressensky, A. A. Alothman, M. Ouladsmane, A. Ahmad and M. S. Javed, *Energies*, 2022, **15**, 9577.

65 C. Yang, H. Chen and C. Guan, *Nanomaterials*, 2019, **9**, 586.

66 T. Chen, Y. Tang, Y. Qiao, Z. Liu, W. Guo, J. Song, S. Mu, S. Yu, Y. Zhao and F. Gao, *Sci. Rep.*, 2016, **6**, 23289.

67 E. S. Agudosi, E. C. Abdullah, A. Numan, N. M. Mubarak, S. R. Aid, R. Benages-Vilau, P. Gómez-Romero, M. Khalid and N. Omar, *Sci. Rep.*, 2020, **10**, 11214.